
Papers

**Computation of energy
for diapycnal mixing in
the Baltic Sea due to
internal wave drag acting
on wind-driven barotropic
currents***

OCEANOLOGIA, 51 (4), 2009.
pp. 461–494.

© 2009, by Institute of
Oceanology PAS.

KEYWORDS

Baltic Sea
Turbulent mixing
Internal waves

CHRISTIAN NOHR^{1,*}
BO G. GUSTAFSSON²

¹ Department of Earth Science,
University of Gothenburg,
Box 460, SE-405 30 Göteborg, Sweden;

e-mail: chno@oce.gu.se

*corresponding author

² Baltic Nest Institute – Stockholm Resilience Centre,
Stockholm University,
SE-106 91 Stockholm, Sweden;

e-mail: bo.gustafsson@stockholmresilience.su.se

Received 23 April 2009, revised 17 November 2009, accepted 24 November 2009.

Abstract

The pathways of energy supply for mixing the deep waters of the Baltic Sea is largely unknown. In this paper, a parameterization of the internal wave drag forces on barotropic motion is developed and implemented into a two-dimensional shallow water model of the Baltic Sea. The model is validated against observed sea levels. The dissipation of barotropic motion by internal wave drag that is quantified from the model results show that breaking internal waves generated by

* This work was funded by the Swedish Research Council under contracts G 600-335/2001 and 621-2003-3425, and by the Swedish Foundation for Strategic Environmental Research via the MARE program. This is publication No. 30 from Tellus – The Centre of Earth Systems Science at the University of Gothenburg.

The complete text of the paper is available at <http://www.iopan.gda.pl/oceanologia/>

wind forced barotropic motions can contribute significantly to diapycnal mixing in the deep water of the Baltic Sea.

1. Introduction

The Baltic Sea is a huge fjord-like estuary with a strong permanent haline stratification and long deep-water residence times (Stigebrandt 2001, 2003, Meier 2005). A substantial freshwater surplus in combination with limited ocean exchange makes the Baltic permanently salt stratified. In the main basin, the Baltic proper, the halocline is located at a depth of approximately 60 m, and below 125–150 m the water is only exchanged intermittently. A seasonal thermocline is formed at 15–20 m during summer and also during winter if the temperature falls below that of maximum density (see Figure 2, page 472).

A restricted water exchange with the North Sea in combination with a large surface area efficiently filters external high frequency sea level oscillations, and therefore the contribution of tides to sea level variability is insignificant (Stigebrandt 1980a, Samuelsson & Stigebrandt 1996, Gustafsson & Andersson 2001). Thus, tides as a source of energy for diapycnal mixing are excluded in the Baltic Sea. Nonetheless, estimates reveal that the energy supplied to carry out the observed changes in stratification is of the order of 2.1 mW m^{-2} (Liljebladh & Stigebrandt 2000), which is actually of a similar order of magnitude to that recorded in smaller fjord basins on the Norwegian coast, which are subject to strong tidal currents (Stigebrandt & Aure 1989).

A number of processes can contribute to diapycnal mixing in the Baltic Sea. Vertically propagating near-inertial waves driven by variability in the wind field were thought to be of major importance until Liljebladh & Stigebrandt (2000) managed to quantify their contribution to about 0.35 mW m^{-2} . Observations of strong baroclinic eddies in the deep water led to speculation that these might make a substantial contribution to diapycnal mixing (cf. Meier et al. 2006, Stigebrandt et al. 2002 and the references in these papers). This speculation was challenged by Svensson (2005), who estimated from observations that mesoscale eddies do not contribute significantly to diapycnal mixing. Double-diffusive mixing may occur periodically when intrusions of warm, saline waters are interleaved in the stratification (e.g. Kuzmina et al. 2005), but in general this should not be a factor contributing to the overall mixing either, since the absolute majority of deep water is quite strongly salt-stratified. Coastal dynamics may enhance mixing due to up- and downwelling, which is exemplified in Stigebrandt et al. (2002). Döös et al. (2004) estimated a dissipation rate of $0.4\text{--}1.2 \text{ mW m}^{-2}$ by turbulent bottom friction from simulations with

a barotropic numerical model. A portion of these losses could possibly be used for mixing. Axell (1998) estimated from observations of stratification that the energy supply needed for mixing in the deeper deep waters (depth > 150 m) was about 5 and 0.6 mW m^{-2} in the Landsort Deep and Eastern Gotland Basin respectively. He found a strong seasonal cycle that largely follows that of the wind. However, there are still gaps in our understanding of how energy is transferred from the atmosphere to the turbulent mixing in the deep water.

Although conversion of barotropic to baroclinic waves has been under intense focus during the past decade, there are no conclusive ways of quantifying the energy flux. That part of the problem involving the excitation of internal waves over an idealized topography and given stratification is fairly straightforward, but it becomes virtually impossible to solve for a realistic topography and when processes like wave-wave interaction and non-linear dissipation due to breaking waves are included. The importance of small-scale processes is evident from studies of internal tides in fjord basins. For example, Berntsen et al. (2008) demonstrated sub-grid scale closure and resolution dependence in very high resolution (10–100 m) simulations of internal tides with a non-hydrostatic model, and Johnsson et al. (2007) showed experimentally that two very closely spaced sills (about 1 km or $1/7$ of the internal Rossby radius) generated internal tides without interaction. Thus, one has to resort to various extremely simplified parameterizations. In recent quantifications of internal wave drag on barotropic tides using shallow water models, parameterizations based on simple analytical considerations and scale arguments have been used (e.g. Sjöberg & Stigebrandt 1992, Gustafsson 2001, Jayne St. Laurent 2001, Egbert et al. 2004, Nycander 2005, Tanaka et al. 2007). There are also examples of direct numerical simulations of internal tide generation using three-dimensional models (e.g. Niwa & Hibiya 2001, Merrifield & Holloway 2002, Simmons et al. 2004, and several others).

In this paper we investigate the extent to which energy can be transferred from the atmosphere via barotropic motion to turbulent kinetic energy in the deep water. One possibility is that internal waves are generated over a steep topography, as happens with tides in the deep oceans and in sill fjords, and another is that turbulence is generated in the bottom boundary layer. We use a two-dimensional shallow water model forced by observed winds and air pressure fields to estimate the energy loss from the barotropic motion due to internal wave drag and bottom friction. The parameterization of wave drag follows the so-called step model (Stigebrandt 1976, 1980b, 1999 Sjöberg & Stigebrandt 1992, Gustafsson 2001, Johnsson et al. 2007). Opposing the oceanic applications of Sjöberg & Stigebrandt (1992) and Gustafsson

(2001), we expect the dominant influence of the first baroclinic mode, and therefore we must consider the stratification of the whole water column. A generalization of internal wave drag on barotropic currents for arbitrary stratification given by Stacey (1984) is adapted to provide drag force in a two-dimensional shallow water model. The validity of the step model was recently challenged by St. Laurent et al. (2003); primary concerns were the assumption of local non-interacting wave generation at each step and that resolution dependence was found, causing the internal wave generation to decrease as the resolution was increased. We will discuss this further in the discussion section in the light of present results; worth noting, however, are the experiences of Egbert et al. (2004) that the step model gives similar internal wave drag as some other parameterizations.

This paper is structured as follows: the model and its implementation are described in Section 2; the performance of the model is evaluated by comparison with observed sea levels in Section 3. In Section 4 we present the results of the simulations, and the paper ends with a discussion of the results and their implications.

2. Method

2.1. Model description

The model is based on two-dimensional shallow water equations; hence, density variations, non-linear interaction in vertical shear flow and non-hydrostatic pressure are all disregarded. This, of course, severely limits the realism of the results for a basin that is strongly stratified. However, the aim here is not to realistically simulate the vertical current structure, but to make an order of magnitude estimate of the possible energy conversion from atmospherically forced barotropic motion to internal motion, and for this purpose the shallow water approximations will most probably suffice. A more severe limitation of the shallow water equations in the present context is that parameterization of drag from bottom boundary layers becomes rather dubious since the actual bottom near currents might not be related to the barotropic flow.

The numerical scheme follows closely the classic model by Arakawa & Lamb (1981). The following form of the momentum equations are discretized,

$$\frac{\partial \mathbf{v}}{\partial t} + q\mathbf{k} \times \mathbf{v}^* + \nabla(K + \Phi) = \frac{\mathbf{F}}{h}, \quad (1)$$

where h is height of the water column, \mathbf{v} is the velocity vector, $\mathbf{v}^* = \mathbf{v}h$ is

the flow vector and $K = \frac{1}{2}\mathbf{v}^2$ is the specific kinetic energy. The potential vorticity q is defined as

$$q = \frac{\zeta + f}{h}, \tag{2}$$

where ζ is the vorticity and f is the Coriolis parameter, which in this case is considered constant ($f = 1.2 \times 10^{-4} \text{ s}^{-1}$). The pressure Φ is given by

$$\Phi = g(h - D) + \frac{P_a}{\rho_0}, \tag{3}$$

where $g = 9.8 \text{ m s}^{-2}$ is the acceleration due to gravity, D is the equilibrium water depth, P_a is the atmospheric pressure and $\rho_0 = 1010 \text{ kg m}^{-3}$ is the reference density of sea water. The body force \mathbf{F} consists of three parts: the wind force \mathbf{F}_{wind} , bottom drag force \mathbf{F}_{b} and internal wave drag force \mathbf{F}_{w} .

The sea surface height is determined from the continuity equation

$$\frac{\partial h}{\partial t} + \nabla \cdot \mathbf{v}^* = 0. \tag{4}$$

The spatial discretization is done on a uniform C-grid and following the Arakawa-Lamb scheme (Arakawa & Lamb 1981), which ensures energy and potential enstrophy conservation. The Arakawa-Lamb scheme requires a computational boundary condition on the tangential velocity at the solid boundary, for which we used a free-slip condition. The temporal evolution is computed with a third-order Runge-Kutta solver following Williamson (1980). Body forces are applied explicitly.

Experimentally the drag force due to small-scale flow separation and bed friction can be estimated from the current velocity squared at a fixed height above the sea bed and a drag coefficient that depends on the structure of the sea bed (e.g. Dyer 1986, Soulsby 1997). The first-order approximation is to use this parameterization for the drag loss to the turbulent bottom boundary layer \mathbf{F}_{b} of the barotropic currents as well,

$$\mathbf{F}_{\text{b}} = -C_d|\mathbf{v}|\mathbf{v}, \tag{5}$$

where C_d is a dimensionless drag coefficient. There are frequent examples of the use of the quadratic drag law in ocean tidal models (e.g. Egbert et al. 2004, Arbic et al. 2004, Tanaka et al. 2007, Weis et al. 2008). In a classic variant of equation (5), commonly used in shelf seas applications, the drag coefficient is a more or less weak function of depth through the introduction of the depth-dependent Chézy coefficient or Manning number (e.g. Verboom et al. 1992, Soulsby 1997, Umgiesser 1997, Jakobsen et al. 2002). We use

equation (5) with a constant drag coefficient, although we will investigate the sensitivity of the results to varying values on the coefficient.

2.2. Derivation of the internal wave drag force

The basic assumption for the derivation of the wave drag parameterization is that the depth changes abruptly from one grid cell to another, thus forming a step, and that velocity must be zero at the vertical wall defined by the step. Internal waves are added to satisfy this boundary condition. The step-model was originally proposed for sill fjords, where the sill itself constitutes the step (Stigebrandt 1976, 1980b), but was generalized to a discrete two-dimensional grid of sea floor by Sjöberg & Stigebrandt (1992). Stacey (1984) generalized the model by Stigebrandt (1976, 1980b) to arbitrary continuous stratification. We use the work of Stacey (1984) to formulate wave drag in the shallow water model.

We show the derivation of the internal wave drag parameterization in the x -direction, since the derivation of the drag in the y -direction is completely analogous. All effects of the Earth's rotation on the internal waves are disregarded; the justification and consequences of this will be discussed later in this paper (see Section 5).

Consider two adjacent grid cells, one deeper with depth H_b and one shallower with depth d . The velocity in the deeper grid cell is given by the superposition of a barotropic wave defined by velocity amplitude u_0 , frequency ω and wave number k_0 , and an infinite number of internal wave modes $\hat{u}_n(z)$ of amplitudes a_n and wave numbers k_n :

$$u(x, z, t) = u_0 \cos(\omega t + k_0 x) + \sum_{n=1}^{\infty} a_n \hat{u}_n(z) \cos(\omega t + k_n x). \quad (6)$$

We assume that no internal waves are generated in the shallower grid cell and therefore the velocity in the shallower grid cell is barotropic with amplitude u_s . The boundary condition at the step ($x = 0$) becomes

$$u_0 + \sum_{n=1}^{\infty} a_n \hat{u}_n(z) = \begin{cases} u_s & 0 \geq z \geq -d \\ 0 & -d > z \geq -H_b \end{cases}. \quad (7)$$

Since the internal wave modes \hat{u}_n are zero in the mean and the orthogonal, the amplitudes are given by

$$a_n = u_s \frac{\int_{-d}^0 \hat{u}_n dz}{\int_{-H_b}^0 \hat{u}_n^2 dz}. \quad (8)$$

Horizontal and vertical modes are related via the continuity equation

$$\hat{u}_n = \frac{1}{k} \frac{d\hat{W}_n}{dz}. \quad (9)$$

The vertical structure of the modes for arbitrary continuous stratification can be found by solving the following vertical velocity eigenvalue problem

$$\frac{d^2\hat{W}_n}{dz^2} + \frac{N^2}{c_n^2}\hat{W}_n = 0, \quad (10)$$

where $N^2 = -\frac{g}{\rho} \frac{d\rho}{dz}$ is the buoyancy frequency (squared) and c_n the wave speed of mode n . The boundary conditions are

$$\hat{W}_n(0) = \hat{W}_n(-H_b) = 0. \quad (11)$$

Thus, the horizontal velocity amplitudes (eq. (8)) can be calculated from equations (9) and (10), and working out the energy density of each mode from the amplitudes is straightforward:

$$E_n = \frac{\rho}{2} \frac{u_s^2 \hat{W}_n(-d)^2}{\int_{-H_b}^0 \left[\frac{d\hat{W}_n}{dz} \right]^2 dz}. \quad (12)$$

Note that the energy density does not depend on the normalization of \hat{W}_n since any scale factor is eliminated. The energy flux radiating with internal waves (per unit width) away from the step is given by

$$\varepsilon = \sum_{n=1}^{\infty} c_n E_n, \quad (13)$$

where c_n is the group speed, which is equal to the phase speed since we are only considering long waves. Dissipation from barotropic motion in the x-direction in the shallow water model, say ε_{SH} , is given by

$$\varepsilon_{SH} = \rho u_i F_w^x \Delta s, \quad (14)$$

where u_i is the velocity, F_w^x the drag force and Δs the grid spacing. Following the definition of the Arakawa C-grid, the velocity u_i is defined at the average depth of the two adjacent grid cells. By neglecting differences in sea

surface elevation we can express the velocity in the shallower grid cell u_s in the model velocity u_i ,

$$u_s d = u_i \frac{1}{2} (H_b + d). \tag{15}$$

By equating ε_{SH} with $-\varepsilon$ and substituting u_s with u_i we get the following expression for the wave drag in the x-direction:

$$F_w^x = -\frac{u_i}{2\Delta s} \left(\frac{H_b + d}{2d} \right) \sum_{n=1}^{\infty} c_n \frac{\hat{W}_n(-d)^2}{\int_{-H_b}^0 \left[\frac{d\hat{W}_n}{dz} \right]^2 dz}. \tag{16}$$

The baroclinic drag coefficient $r_w^x = \frac{F_w^x}{u_i}$ at grid point i, j can be defined as

$$r_w^x = -\frac{1}{2\Delta s} \left(\frac{H_b + d}{2d} \right) \sum_{n=1}^{\infty} c_n \frac{\hat{W}_n(-d)^2}{\int_{-H_b}^0 \left[\frac{d\hat{W}_n}{dz} \right]^2 dz}, \tag{17}$$

where the depths are calculated from the equilibrium depths of the adjacent grid cells, and \hat{W}_n and c_n are computed for the deeper of the two cells.

A completely analogous expression is derived for baroclinic drag in the y-direction. To write the wave drag in vector notation we can define a matrix \mathbf{R}_w that has the drag coefficients r_w^x and r_w^y for the x- and y-directions respectively as diagonal elements, that is,

$$\mathbf{F}_w = \mathbf{R}_w \cdot \mathbf{v}. \tag{18}$$

2.3. Derivation of the approximate drag force

In an approximately two-layer stratified basin like the Baltic Sea, it may be possible to use a simplified form of the wave drag. It can easily be shown that the total energy density of the internal waves is independent of the stratification (see Sjöberg & Stigebrandt 1992). In our notation the total internal wave energy density becomes

$$E = \frac{\rho}{2} u_s^2 d \left(1 - \frac{d}{H_b} \right). \tag{19}$$

If we use equation (15) and define $H = \frac{1}{2}(H_b + d)$ and $\Delta H = \frac{1}{2}(H_b - d)$, the energy density can be written as

$$E = \rho u_i^2 \frac{1}{1 - \left(\frac{\Delta H}{H}\right)^2} \Delta H. \quad (20)$$

If the first mode dominates, one can estimate the energy flux of the internal waves by using the group speed of that mode, say c_g , and derive an expression for the wave drag by equating the energy flux of the internal waves and the dissipation in the barotropic model, as in Section 2.2. The result is

$$F_w^x = -c_g \frac{1}{1 - \left(\frac{\Delta H}{H}\right)^2} \frac{\Delta H}{\Delta s} u_i. \quad (21)$$

There are practical advantages if this can be used, since only an estimate of the first mode group speed is needed instead of continuous density profiles. For long waves the group speed can be approximated by

$$c_g = \sqrt{g \frac{\Delta \rho}{\rho} h_p \left(1 - \frac{h_p}{H_b}\right)}, \quad (22)$$

where h_p is the depth of the pycnocline and $\Delta \rho$ a typical difference between surface and deep water density. Naturally $c_g = 0$ if $h_p \geq H_b$.

2.4. Implementation

Three equidistant grids, 1×1 nm, 2×2 nm and 4×4 nm, were interpolated from the bathymetry with an original resolution of 2 minutes of longitude and 1 minute of latitude (Seifert et al. 2001). The 2×2 nm bathymetry (shown in Figure 1) was used in all simulations, except those testing the sensitivity of the results to changed horizontal resolution. A sponge zone was added at the open boundary towards the North Sea by adding 20 identical points westwards (see Figure 1). In this zone, velocity and surface elevation were relaxed towards the external boundary condition following the flow relaxation method devised by Martinsen & Engedahl (1987). The open boundary towards the North Sea is forced by hourly sea level observations from Hirtshals. We assume that the sea level changes gradually from the observed level at the coast with the length scale of the local Rossby radius. The velocity is specified according to Flather (1976). Thus, the equations for sea level and currents along the open boundary are

$$\frac{d\eta}{dy} = -\frac{f}{\sqrt{gD}} \eta \quad (23)$$

and

$$u = \sqrt{\frac{g}{D}}\eta. \quad (24)$$

In the equation for sea level η , y is directed along the open boundary, f is the Coriolis parameter, g is the acceleration due to gravity and D is the depth.

The model is forced by geostrophic wind and air pressure fields with a time resolution of 3 hours and a grid resolution of $1^\circ \times 1^\circ$. The database is available from the BALTEX Hydrological Data Centre (BHDC), and it is here interpolated to fit the grid of the model domain. The wind stress

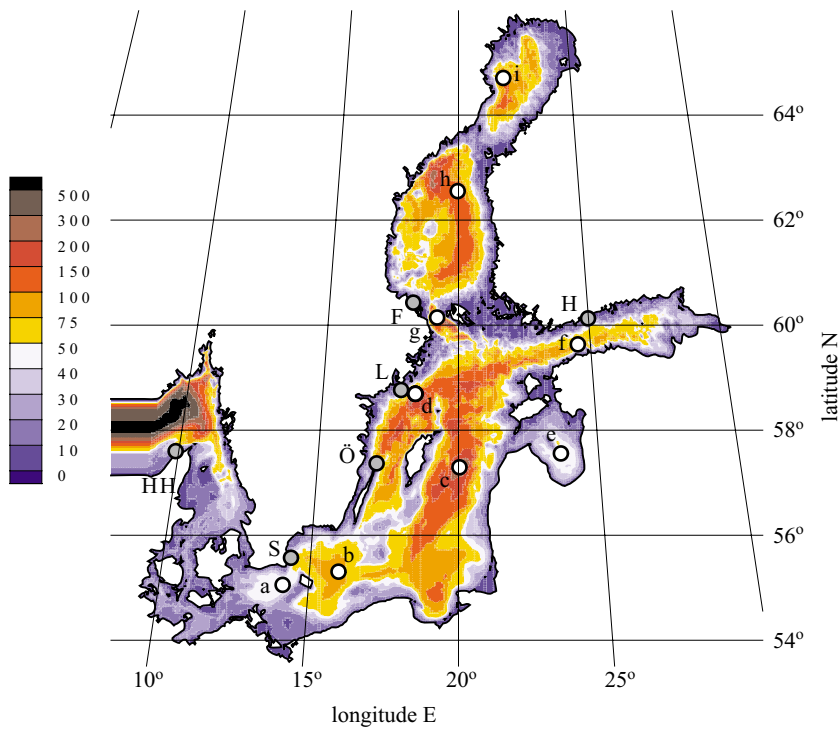


Figure 1. The 2×2 nm model bathymetry, including the added sponge zone at the border to the North Sea. The locations of the tide gauges used in this paper are indicated. The abbreviations are: HH = Hirtshals, S = Simrishamn, Ö = Ölands Norra Udde, L = Landsort, F = Forsmark and H = Helsinki. The hydrographic stations used for calculating dynamic wave modes are indicated by light grey circles and the legend for the lower case letters is a = BY2, b = BY5, c = BY15, d = BY31, e = Gulf of Riga, f = LL11, g = F64, h = US5B and i = F9. The depths in the colour scale are given in metres

is calculated from the geostrophic wind in two steps. First, the geostrophic wind is reduced to 10 m wind using $\mathbf{w}_{10} = \mathbf{M} \cdot \mathbf{w}_g$. The reduction is found by comparison with wind observations in central Baltic proper. The conversion matrix used is

$$\mathbf{M} = \begin{bmatrix} 0.645 & 0.215 \\ 0.229 & 0.645 \end{bmatrix}. \quad (25)$$

The wind force is calculated from

$$\mathbf{F}_{\text{wind}} = \frac{\rho_a}{\rho_0} C_a |\mathbf{w}_{10}| \mathbf{w}_{10}, \quad (26)$$

where $\rho_a = 1.25 \text{ kg m}^{-3}$ is the density of air. The drag coefficient, C_a , is computed following Smith (1980), i.e.

$$C_a = \begin{cases} 1.1 \times 10^{-3} & |\mathbf{w}_{10}| < 6 \text{ m s}^{-1} \\ (0.73 + 0.063|\mathbf{w}_{10}|) \times 10^{-3} & |\mathbf{w}_{10}| \geq 6 \text{ m s}^{-1} \end{cases}. \quad (27)$$

The main simulation period was chosen to be 1 January 1992–31 December 1992, a year with no major deep-water inflows. As this was also a warm year with only limited ice cover, only limited effects of sea ice on the momentum fluxes at the sea surface are expected. As a crude estimate of the variability due to strength of stratification and interannual variability in the winds, we also performed simulations for 1 January 1995–31 December 1995. The stratification was much stronger in 1995 than in 1992.

In our standard case we use a bottom drag coefficient $C_d = 3 \times 10^{-3}$. However, a series of simulations are performed varying the bottom drag coefficient C_d , spatial resolution, wind stress and without wave drag. Also, the simplified drag formula is tested.

2.5. Calculation of the baroclinic drag coefficient

Observed density profiles from 9 oceanographic stations (locations shown in Figure 1) are used to calculate the vertical dynamic modes \hat{W}_n and the corresponding phase speeds c_n . The data from each station are assumed to be representative for a part of the Baltic Sea so that in all, the 9 stations cover the model domain within the sills. Figure 2 shows typical winter and summer stratification in three regions in the Baltic Sea: the Gotland Deep (BY15), the Landsort Deep (BY31) and the Åland Sea (F064). A characteristic summer thermocline is seen at about 20 m and a perennial pycnocline at about 60 m depth. Wave drag is not computed for the Skagerrak and Kattegat. The procedure for calculating the wave

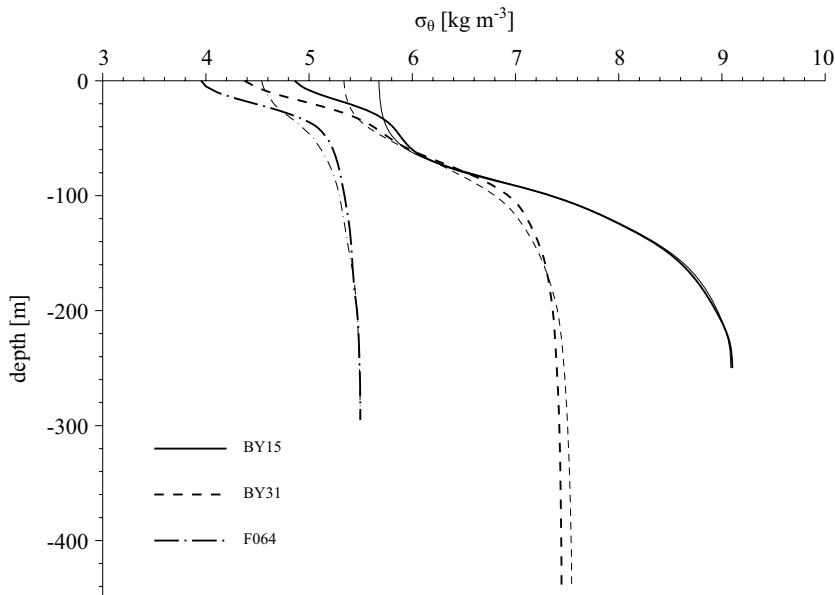


Figure 2. Examples of typical vertical winter and summer stratifications from the Gotland Deep (BY15), Landsort Deep (BY31) and Åland Sea (F064). Grey lines – summer stratification, black lines – winter stratification

drag coefficients \mathbf{R}_w are as follows: the depths H_b and d are determined for each grid cell pair. The buoyancy frequency profile N is calculated either as a summer (mean for the months May–August) or a winter (mean for the months November–March) profile from the oceanographic station in the vicinity of the grid cell. Summer and winter mean profiles are calculated using data from the two simulation periods. Owing to the sparse data coverage at stations BY31, F064, LL11 and RIGA, data from 1988–92 and 1993–97 had to be used. The vertical resolution is 5 m and linearly interpolated to 1 m resolution. The profiles are truncated at the depth of the deeper grid cell, i.e. at H_b . The vertical dynamic modes problem is solved using numerical integration techniques, in this case Runge-Kutta with the shooting method. The Runge-Kutta method uses a trial step to the midpoint of an interval to cancel out lower-order error terms. The shooting method is a method for solving a boundary value problem by reducing it to the solution of an initial value problem; the analysis is described in e.g. Press et al. (1992). The 10 first modes are calculated.

In the calculation with the approximate wave drag formula (eq. (21)), we used a constant $\Delta\rho = 3 \text{ kg m}^{-3}$ and $h_p = 65 \text{ m}$ throughout the Baltic Sea, although the figures are representative for the Baltic proper only.

3. Model performance

Model results are validated against hourly data from five sea level monitoring stations: Simrishamn, Landsort, Ölands Norra Udde, Helsinki and Forsmark (locations shown in Figure 1). The stations are selected to cover the main parts of the Baltic proper. The time-series of simulated and observed sea levels for the whole simulation are drawn in Figure 3.

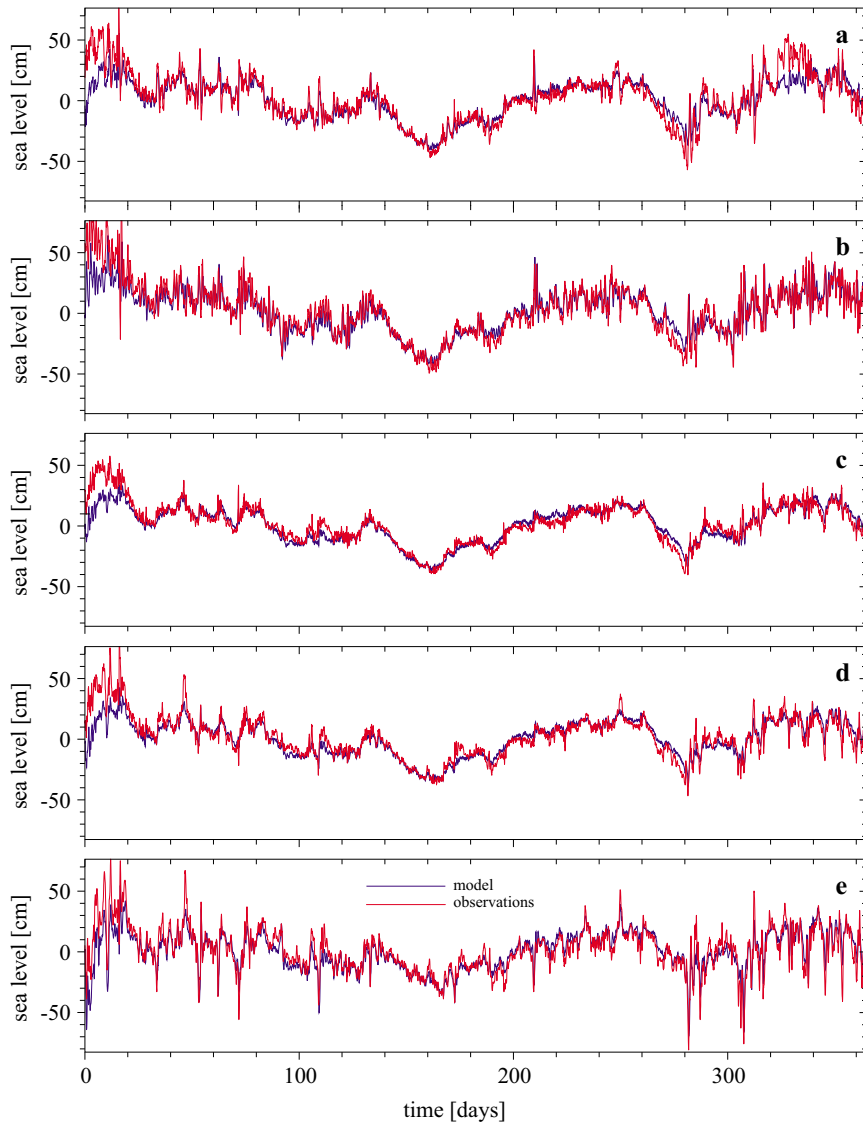


Figure 3. Observed and modelled sea levels at Forsmark (a), Helsinki (b), Landsort (c), Ölands Norra Udde (d) and Simrishamn (e)

Since the model starts with zero sea level everywhere, there is a spin-up period of about 20 days before the volume of the Baltic is adjusted to the boundary conditions. The model captures most of the sea level variations, but generally underestimates the magnitude of short, extreme sea level events. The high frequency variability is larger in the Bay of Bothnia and Gulf of Finland (Forsmark and Helsinki, Figure 3a and 3b), and in the southern Baltic (Simrishamn, Figure 3e) than in the central Baltic (Landsort, Figure 3c) owing to the wind set-up. There is a spurious discrepancy between the model and observations at about 320–340 days at Forsmark that is difficult to explain as the model performs well at other locations during this time.

Power spectra of modelled and observed sea levels at the five sea level monitoring stations are shown in Figure 4. The computation was done with a 256 h long Hanning window with 50% overlap, which gave a total of 67 independent determinations. At all positions, semidiurnal tides ($M_2 = 12.42$ h) are seen in both the observed and simulated sea levels. There is a tendency towards a diurnal tide in some of the sea level observations that does not show up in the model results, as the diurnal tidal signal is primarily locally driven and not imported from the North Sea (Jönsson et al. 2008). As indicated above in the time-series plots (Figure 3), the model underestimates variance in the high-frequency part of the spectrum. In relative terms, the performance at high frequencies is better at Forsmark and Simrishamn than at Landsort and Ölands Norra Udde. The probable cause is that the variability close to the nodal line of oscillations depends to a larger degree on small-scale features in forcing and topography than on those near the anti-nodes. The time resolution of the forcing prevents the model from capturing periods shorter than 3 hours. A sea level response longer than 10 hours has an energy comparable with the observations, and at some stations the model results show comparable energy levels for periods as short as 4–5 hours. Figure 5 shows coherence and phase spectra. Even though power density spectra indicate that the model produces a significant amount of energy at a relatively high frequency, coherence decreases for periods shorter than 20 h and is less than ca 0.5 for periods shorter than 10 hours. The coherence between modelled and observed sea levels is high and the phase differences are small at all stations for periods longer than 20 hours. For the really long periods the phase difference increases somewhat. Especially in the central Baltic proper, namely Landsort and Ölands Norra Udde, observed sea levels have a daily cycle that is not picked up by the model. The driving forces behind the daily cycle are evidently not resolved by the model.

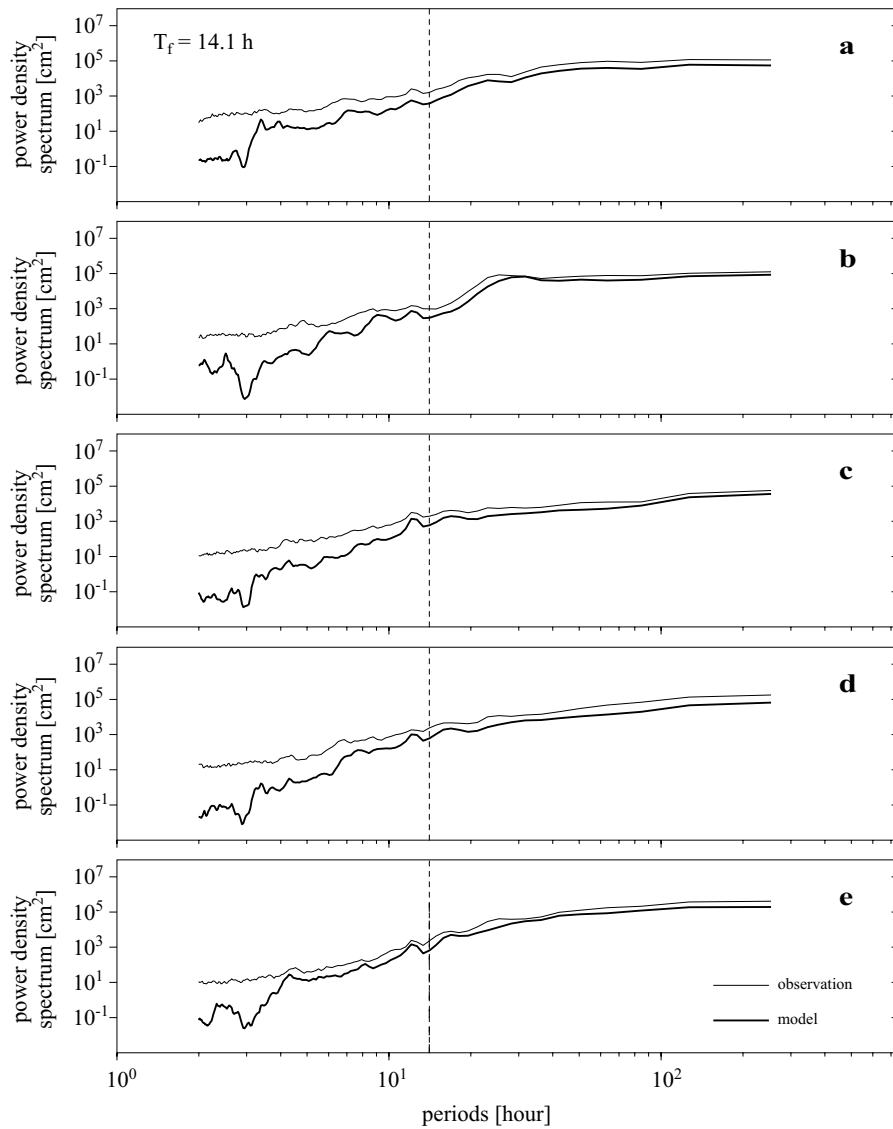


Figure 4. Spectra of simulated and observed sea levels at Forsmark (a), Helsinki (b), Landsort (c), Ölands Norra Udde (d) and Simrishamn (e)

A quantitative skill assessment of the standard case and a number of simulations with varying bottom drag coefficient, wind forcing and wave drag is made in terms of correlation squared r^2 and root mean squared (RMS) error. To avoid corruption from the spin-up of the model all statistics are computed excluding the initial 30 days, leaving 8040 data points for the statistics. Since changing friction and resolution of the model greatly

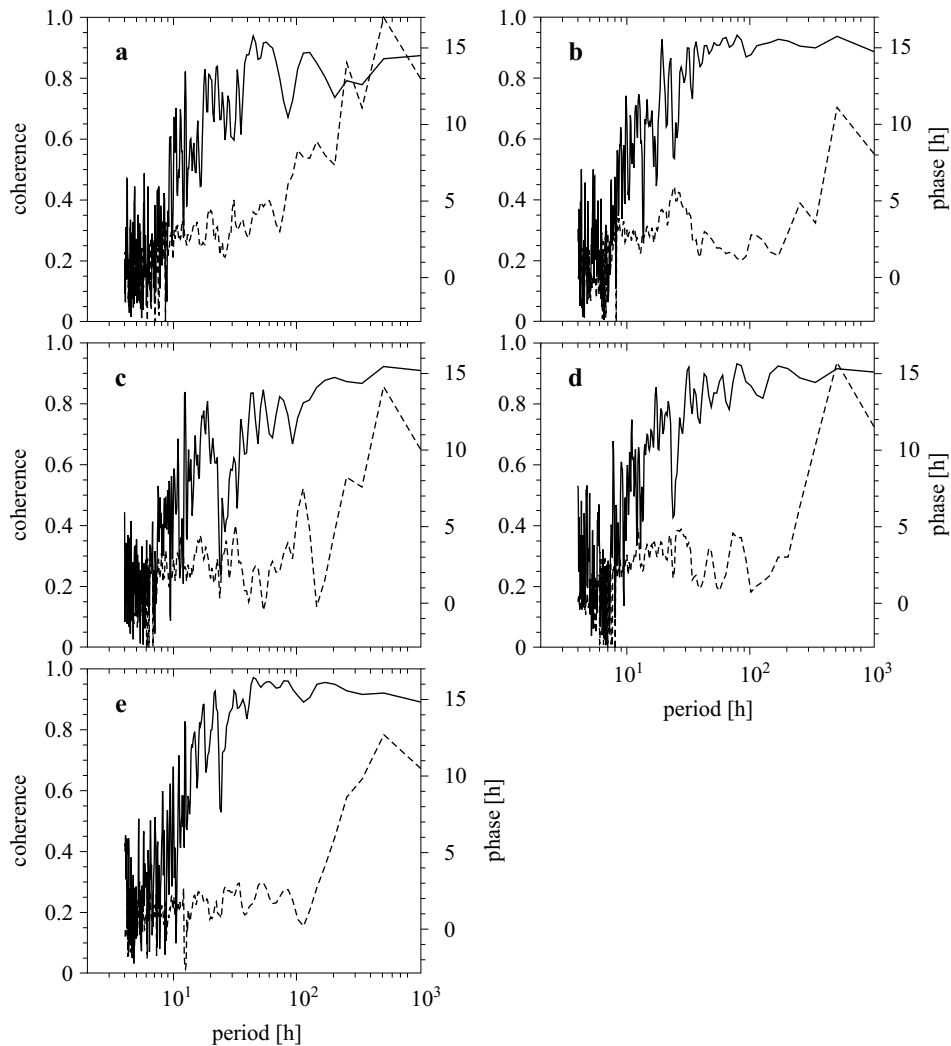


Figure 5. Coherence and phase spectra between observed and simulated sea levels at Forsmark (a), Helsinki (b), Landsort (c), Ölands Norra Udde (d) and Simrishamn (e). Solid lines – coherence, dashed lines – phase spectra

influence the filling and emptying of the Baltic through the Danish Straits, we also made a simple estimate of the high-frequency part of the error that to a larger degree reflects the effects of changing parameters on the internal oscillations of the Baltic Sea (e.g. Samuelsson & Stigebrandt 1996). The high-frequency part of the RMS error is estimated by first cutting the time-series into 240 h long time-slices, then computing the error variance for each time-slice, and finally computing the RMS error from the average

of these variances, i.e.

$$RMS_h = \sqrt{\frac{1}{M} \sum_{m=1}^M \frac{1}{N} \sum_{n=1}^N \left(\eta_{n,m}^{\text{mod}} - \bar{\eta}_m^{\text{mod}} - \eta_{n,m}^{\text{obs}} + \bar{\eta}_m^{\text{obs}} \right)^2}, \quad (28)$$

where η^{mod} and η^{obs} are the modelled and observed sea levels respectively. $N = 240$ is the number of observations in each of the $M = 33$ slices. Barred quantities are averaged for each slice. In addition to the correlation and RMS computations, we performed a Kruskal-Wallis non-parametric ANOVA test to discover the simulations that gave a significantly different result compared to the simulation with the standard parameter setting (i.e. $p < 0.05$ for the null hypothesis that they are similar). We also performed the test between simulations and observations, finding that all the simulation results were significantly different from the observations.

The correlations and RMS errors for all runs are summarized in Tables 1 and 2. The results of the Kruskal-Wallis test are also listed in Table 1, which shows that only a few of the test cases differ significantly from the control

Table 1. Correlation (r^2) between hourly observed and modelled sea level time-series (8040 data points) from each of the simulations. The highest correlations are given in bold. The cases that are significantly different ($p < 0.05$ for the null hypothesis that they are similar) from the standard case are marked with an asterisk. The 1995 simulation is not included in the statistical analysis

Stations	Forsmark	Helsinki	Landsort	Ölands Norra Udde	Simrishamn
$C_d = 3 \times 10^{-3}$	0.907	0.913	0.947	0.926	0.893
$C_d = 1 \times 10^{-3}$	0.908*	0.902*	0.939*	0.920*	0.874
$C_d = 2 \times 10^{-3}$	0.911	0.912	0.947	0.926	0.889
$C_d = 4 \times 10^{-3}$	0.901	0.911	0.944	0.922	0.894
$C_d = 6 \times 10^{-3}$	0.890	0.904	0.937*	0.914*	0.892
$C_d = 8 \times 10^{-3}$	0.879*	0.897*	0.929*	0.905*	0.886*
no wave drag	0.907	0.912	0.947	0.926	0.895
approx. wave drag	0.906	0.915	0.947	0.926	0.895
$\mathbf{F}_w + 25\%$	0.907	0.916	0.951	0.936	0.913
$\mathbf{F}_w + 50\%$	0.905	0.915	0.952	0.943	0.923
$\mathbf{F}_w + 75\%$	0.894	0.906	0.950	0.944	0.921
4×4 nm	0.854	0.861	0.902*	0.876*	0.878
1×1 nm	0.909	0.915	0.949	0.928	0.895
1995	0.926	0.921	0.926	0.915	0.902

Table 2. RMS error (in cm) computed from hourly observed and modelled sea levels (8040 data points) from each of the simulations. The RMS errors computed from 240 h time-slices are given in parentheses. Lowest RMS errors are indicated in bold (1995 excepted). The standard deviations of the observed time series, both in total and using 240 h slices, are indicated for comparison

Stations	Forsmark	Helsinki	Landsort	Ölands Norra Udde	Simrishamn
Standard dev.	18.5 (9.27)	18.0 (10.1)	14.5 (6.11)	14.6 (7.77)	16.5 (12.3)
$C_d = 3 \times 10^{-3}$	7.83 (5.86)	7.33 (6.60)	4.71 (3.29)	5.57 (4.33)	7.42 (6.25)
$C_d = 1 \times 10^{-3}$	7.90 (6.12)	8.28 (7.02)	6.05 (3.55)	6.58 (4.18)	8.43 (5.99)
$C_d = 2 \times 10^{-3}$	7.61 (5.86)	7.45 (6.66)	4.95 (3.23)	5.72 (4.16)	7.64 (6.06)
$C_d = 4 \times 10^{-3}$	8.14 (5.90)	7.44 (6.62)	4.78 (3.41)	5.66 (4.51)	7.40 (6.42)
$C_d = 6 \times 10^{-3}$	8.74 (6.01)	7.82 (6.69)	5.18 (3.65)	6.04 (4.79)	7.58 (6.70)
$C_d = 8 \times 10^{-3}$	9.24 (6.11)	8.23 (6.76)	5.63 (3.83)	6.46 (5.00)	7.84 (6.91)
no wave drag	7.82 (5.84)	7.38 (6.66)	4.72 (3.30)	5.54 (4.31)	7.36 (6.19)
approx. wave drag	7.85 (5.90)	7.26 (6.54)	4.72 (3.30)	5.56 (4.33)	7.37 (6.22)
$\mathbf{F}_w + 25\%$	7.76 (5.92)	7.26 (6.66)	4.61 (3.26)	5.21 (4.07)	6.79 (5.70)
$\mathbf{F}_w + 50\%$	7.88 (6.13)	7.43 (6.90)	4.62 (3.30)	4.99 (3.91)	6.55 (5.55)
$\mathbf{F}_w + 75\%$	8.39 (6.76)	8.12 (7.64)	4.84 (3.52)	5.03 (4.00)	6.97 (6.05)
4 × 4 nm	10.25 (6.24)	9.43 (7.10)	6.81 (4.14)	7.52 (5.20)	8.29 (6.92)
1 × 1 nm	7.78 (5.88)	7.24 (6.54)	4.62 (3.26)	5.48 (4.32)	7.36 (6.24)
1995	7.78 (5.49)	8.59 (6.70)	6.74 (3.93)	7.57 (5.82)	8.03 (6.66)

run. The correlation between observed and simulated sea levels is generally quite high, and RMS errors are less than 50% of the standard deviation of the observed sea level records. The highest correlation and lowest RMS errors were found at Landsort and the second-highest and -lowest at Ölands Norra Udde for the cases with 25%–50% increased wind stress. It is quite evident that increased wind forcing improves the correlation for sea level stations within the Baltic proper. However, for Forsmark, 25 and 50% increases in wind stress did not change the correlation at all, and for a 75% increase the correlation decreased. When the bottom drag coefficient was changed from 1 to 8×10^{-3} , highest correlations and lowest RMS errors were found for the standard case for all the stations, except Forsmark and Simrishamn where the extremes occurred for $C_d = 2 \times 10^{-3}$ and $C_d = 4 \times 10^{-3}$ respectively. It is evident that bottom stress on the flows through the Åland Sea is important for the sea level variations at Forsmark, and minimal RMS error for high frequencies only are in general shifted towards a lower bottom drag coefficient, $C_d = 2 \times 10^{-3}$. The most

extreme difference is at Simrishamn where the overall RMS error was lowest for $C_d = 4 \times 10^{-3}$ and the lowest-high frequency RMS error was found for $C_d = 1 \times 10^{-3}$. Increasing the grid resolution from 2×2 to 1×1 nm produced only trivial changes in the correlation, but lowering the resolution to 4×4 nm gave a significant reduction. The difference between the total and high frequency RMS errors indicate that lowering the resolution reduces the accuracy primarily at low frequencies. We can therefore conclude that the flows through the Danish Straits are less correctly simulated in the coarse resolution case. The simulation with no wave drag and the approximate wave drag (eq. (21)) gives no change in the correlation compared to the standard case, which indicates that wave drag has only a slight influence on coastal sea levels. The 1995 simulation reproduces sea levels with the same level of accuracy as the 1992 one.

4. Results

4.1. Dissipation of energy from barotropic motion

The horizontal distribution of the time-averaged dissipation of energy from the barotropic motion by internal wave drag and bottom friction is drawn in Figure 6. The temporally averaged dissipation by wave drag is large along the 50 m isobath off the eastern and north-western coasts of the Baltic proper (Figure 6a). This enhancement is possible due to the vertical distribution of depths, the stratification and also the simulated coastal jets. The results are not shown here but they are in accordance with Zhurbas et al. (2006). The spatial distribution is quite patchy and a number of hot spots can be identified, usually associated with abrupt changes in the bathymetry. For example, the entrance area of the Gulf of Finland seems to be one of these. Closer inspection of the simulated currents (not shown) reveals a shallow coastal jet flowing northwards along the eastern coast of the Baltic proper. When the coastal current enters the Gulf of Finland the barotropic motion seems to dissipate within a short distance. As expected, bottom stress is high at shallow depths close to the shore. Especially along the eastern coasts of the Baltic proper, the coastal current mentioned above gives rise to a large bottom stress. This is also the case in the southern Baltic Sea, where coastal currents are strong. Further, in narrow straits like the Åland Sea, and not least, in the narrow Danish straits and Kattegat (not shown), dissipation by bottom stress is large due to the strong currents.

We have computed averages from four areas, indicated by the letters A–D in Figure 6. Areas A and B cover the two deepest basins, the Landsort Deep (monitoring station BY31) and the Eastern Gotland basin (BY15),

respectively. Area C covers the Baltic proper without the marginal gulfs and Box D covers the Åland Sea. The energy losses due to internal wave drag and bed friction averaged in the different areas are presented in Table 3. To get an overview of the difference between shallow and deep areas, we computed the average dissipation due to internal wave drag and bottom stress in selected depth intervals. The dissipation by bottom stress is much smaller in deeper than in shallower water, as expected from the above spatial distributions. The dissipation due to wave drag seems to be of a similar magnitude in deep water as in shallow water areas, which makes the relative contribution of internal wave drag to the loss of barotropic energy larger in deep water areas. The detailed results for the different areas are quite different. In the Baltic proper as a whole (area C), the mean dissipation to internal waves is 0.23 mW m^{-2} , which is only a fraction of the dissipation by

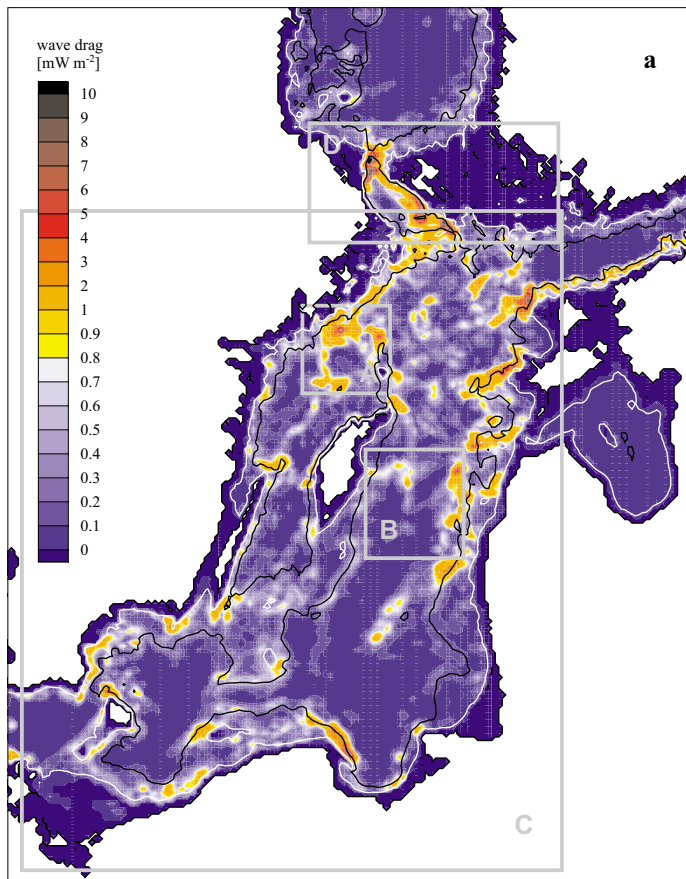


Figure 6. (continued next page)

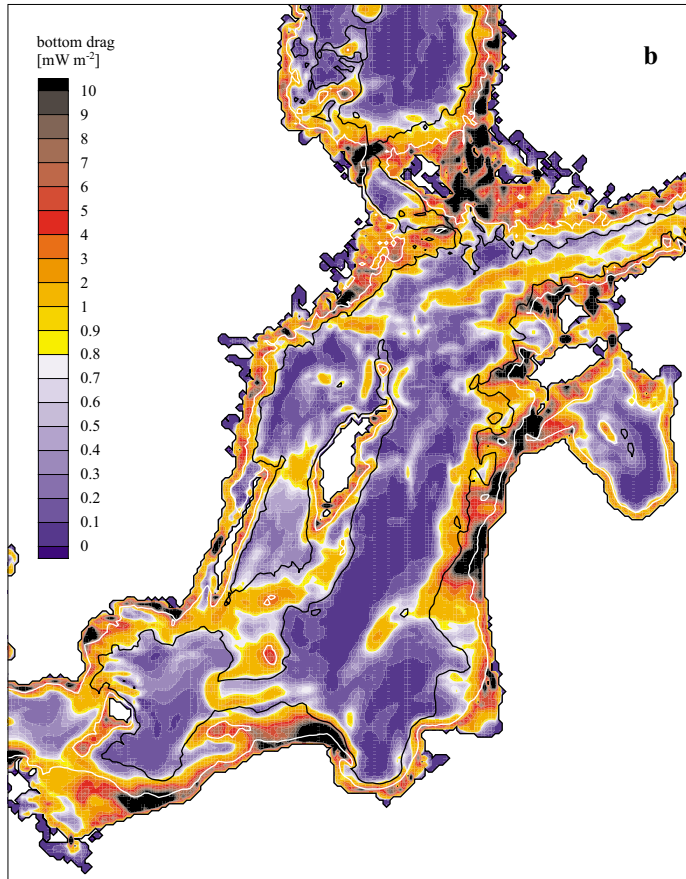


Figure 6. Spatial variation of time-averaged dissipation by internal wave drag (panel a) and by bottom stress (panel b). Also indicated are depth contours for 20 m (white) and 50 m (black). Area A covers the Landsort Deep, B the Gotland Deep, C the Baltic proper and D the Åland Sea

bottom stress (1.3 mW m^{-2}). However, dissipation by wave drag remains approximately constant for all depth intervals, so that in waters deeper than 50 m the two causes of dissipation are of comparable magnitude ($\sim 0.2\text{--}0.4 \text{ mW m}^{-2}$). The largest dissipation by wave drag is found at greater depths in area D, up to about 2 mW m^{-2} . In areas A and B, where two of the deepest areas are located, dissipation by wave drag is higher or equal to that from bottom stress, even though in area B the dissipation by wave drag decreases with depth for areas deeper than 100 m.

The temporal variability of dissipation by internal wave drag is quite large, which is exemplified by the time-series for area C in Figure 7. The average for the area is shown by a thin dashed line. During strong

Table 3. Spatial and temporal averages of dissipation due to internal wave drag and bottom drag in the standard case. Averages are calculated for sub-areas defined by different depth intervals; the ‘All’ column refers to all depths, i.e. to the whole area

Area	Internal wave drag [mW m^{-2}]					
	All	0–50 m	50–100 m	100–150 m	150–200 m	200–250 m
A	0.61	0.44	0.72	0.62	0.41	0.95
B	0.29	0.32	0.59	0.25	0.15	0.10
C	0.23	0.21	0.24	0.26	0.26	0.28
D	0.43	0.22	1.09	2.08	2.07	0.88

Area	Bottom stress [mW m^{-2}]					
	All	0–50 m	50–100 m	100–150 m	150–200 m	200–250 m
A	1.10	3.15	0.53	0.74	0.38	0.33
B	0.50	1.90	1.25	0.20	0.10	0.11
C	1.55	2.82	0.49	0.36	0.22	0.15
D	4.09	4.74	1.48	1.24	0.76	0.50

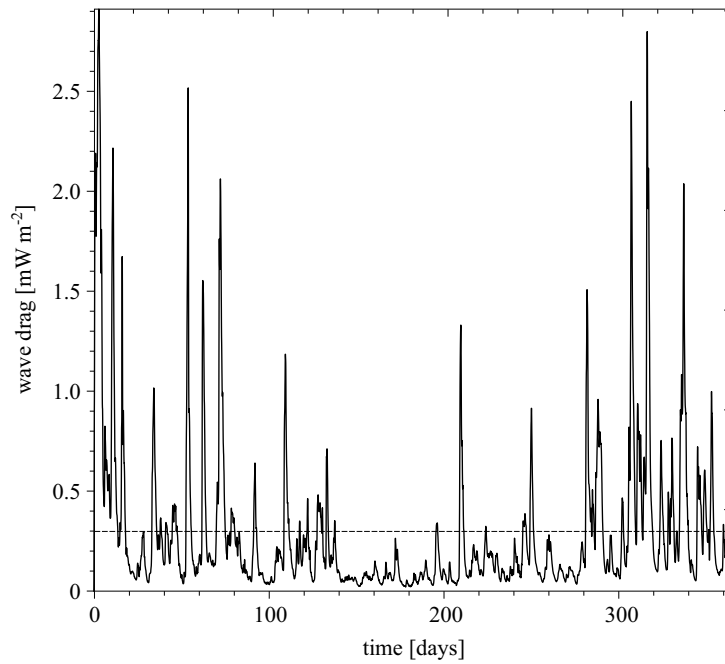


Figure 7. Horizontally averaged dissipation by internal wave drag for box C, the Baltic proper (Fig. 6a). The thin dashed line indicates the annual mean dissipation by internal wave drag (0.23 mW m^{-2})

wintertime events, the internal wave drag reaches levels of almost 3 mW m^{-2} , or a factor of ten larger than the average. The mean duration of periods when the dissipation is larger than average is 44 hours for area C and in total dissipation is above average during slightly less than 30% of the time. The results for the other areas are similar.

The seasonal signal is even more evident from the monthly mean of the dissipation by internal wave drag for areas A–D (see Figure 8). Maximal monthly dissipation is almost one order of magnitude larger than the minimal.

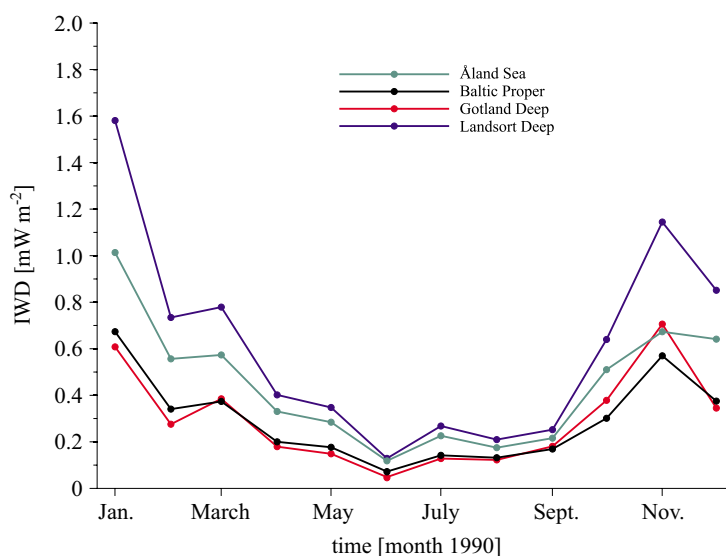


Figure 8. Monthly mean of horizontally averaged dissipation by internal wave drag for the Landsort Deep (area A), the Gotland Deep (area B), the Baltic proper (area C) and the Åland Sea (area D)

4.2. Contribution to mixing

Horizontal averages of dissipation are computed for areas deeper than a specified depth. The dissipation by wave drag and bottom stress as a function of depth is drawn in Figure 9 for areas A, B and D. The dissipation by wave drag is subdivided into the contributions from the 1st and 2nd, and the sum of the 3rd–10th dynamic modes. Under the bold assumption that the dissipation occurring below a certain depth level contributes to mixing only there, and not above that level, we can regard this (Figure 9) as the supply of mechanical energy. In that case, the fraction given by the Richardson flux number ($R_f \approx 0.05\text{--}0.2$) could be used for mixing. We see clearly that the dissipation below 50 m or so is too weak to explain the

total supply needed of some 2.1 mW m^{-2} (Liljebladh & Stigebrandt 2000), mentioned in the Introduction. However, at greater depths the required energy supply for mixing seems to be rather smaller. Axell (1998) computed the energy supply needed to sustain work against the buoyancy forces in the deepest parts of the Landsort Deep (area A) and Eastern Gotland Deep (area B) from changes in density during stagnation periods. Assuming $R_f = 0.05$, Axell (1998, Figure 10) obtained an average energy supply for mixing of about 5 and 0.6 mW m^{-2} to the deep water below 150 m in areas A and B respectively. The model results give respective average dissipations of wave drag of 0.62 and 0.14 mW m^{-2} for those areas below 150 m depth (see Figure 9). Although this is only 12.5% and 25% of the needed supply, it is clearly an indication that processes involving internal wave generation by barotropic currents can be important.

The vertical variation of dissipation due to internal wave drag is quite different in the different areas (Figure 9). In area A the dissipation increases with depth, while a definite decrease to zero is found in area B. This conforms broadly with Axell (1998), who found that the work against buoyancy forces decreased with depth in both areas; however, he found that the decrease started at above 300 m depth in area A, a situation that may not be resolved in the present model. In area D, there is a definite maximum in dissipation around 100 m depth and the profile is quite different from the other two areas. The contribution seems to be dominated by the 1st dynamic mode, most probably because of the strong generation at the two sills delimiting the basin water. The influence from higher order modes becomes prominent at greater depths, especially in area B, where they contribute about 40%, but also in area A.

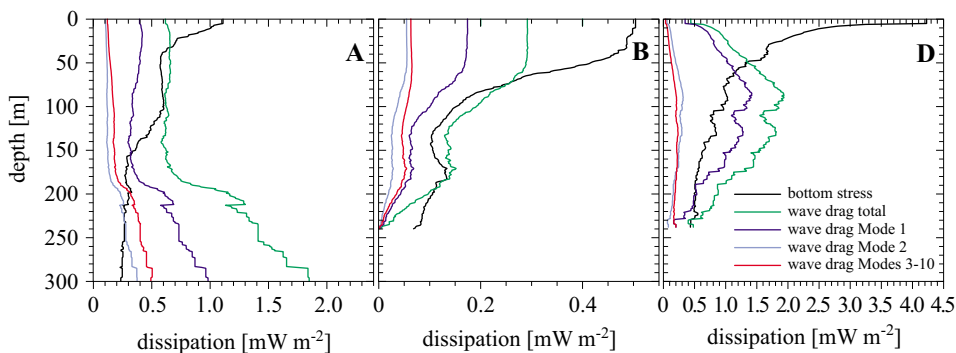


Figure 9. Spatial average of dissipation due to bottom stress and wave drag over areas covering depths greater than the depth on the y-axis. Total wave drag and the contributions from the 1st, 2nd and the sum of 3rd–10th dynamic modes are drawn. There is one panel each for the areas A, B and D as defined in Figure 6

The bottom stress contribution to mixing in deep waters should be interpreted with great caution, since most probably the near-bottom currents here are determined to a large extent by the baroclinic response.

4.3. Sensitivity

There are uncertainties in the parameters and the forcing of the model that could not be fully resolved by comparison with the sea level observations above. Therefore, we make an assessment of the sensitivity of the dissipation results. The averaged dissipations due to wave drag and bottom drag for the different model experiments are shown in Tables 4–7. The experiments with different bottom drag coefficients show that, in general, dissipation by both wave drag and bottom stress decreases with higher drag coefficient. The decrease in dissipation by bottom stress does not apply to area B, however, where instead dissipation increases with increasing drag coefficient. The sensitivity of dissipation by bottom stress to the drag coefficient decreases with depth, while the sensitivity remains high for dissipation by wave drag in deep water. Dissipation by bottom stress is quite sensitive to the absence or the parameterization of internal wave drag. The extreme cases are, for example, in area D, where removing wave drag causes more than a doubling of dissipation by bottom drag at greater depths, and the approximate wave drag reduces it by half. The approximate wave drag causes significantly larger dissipation in deep areas than the full wave drag formulation, showing that it is probably not applicable to estimates of the energy supply to deep water mixing. Increased wind stress increases dissipation due to both wave drag and bed friction. At greater depths, they typically double when the wind stress is increased by 50%.

Dissipation due to wave drag systematically decreases with higher spatial resolution, while changes of dissipation due to bed friction are not systematic. The sensitivity is modest when all depths are included. The changes are larger at greater depths; the most extreme ones are below 200 m in area D, where dissipation due to wave drag decreases by a factor of 4.5 on going from 4×4 nm to 1×1 nm resolution. The deeper regions of area A are less sensitive to horizontal resolution with only modest changes in dissipation. At greater depths in area B decreased dissipation by wave drag seems to be compensated by increased dissipation by bottom stress. The largest decrease is seen from 2 to 1 nm for dissipation due to wave drag, which applies to all areas.

The simulation of 1995 gives a consistently higher dissipation due to both wave drag and bed friction than the 1992 simulation. In area A dissipation is lower at greater depths, and in area C the dissipation due to wave drag shows only small changes or none at all when bed friction

Table 4. Spatial average in area A of dissipation by internal wave drag and bottom stress over sub-areas deeper than the depth given in the table

	Internal wave drag [mW m ⁻²]					Bottom stress [mW m ⁻²]				
	0 m	50 m	100 m	150 m	200 m	0 m	50 m	100 m	150 m	200 m
$C_d = 3 \times 10^{-3}$	0.61	0.65	0.62	0.62	1.17	1.10	0.57	0.59	0.36	0.30
$C_d = 1 \times 10^{-3}$	1.05	1.10	1.02	1.05	2.01	1.19	0.41	0.40	0.26	0.24
$C_d = 2 \times 10^{-3}$	0.76	0.81	0.76	0.77	1.46	1.15	0.52	0.53	0.33	0.29
$C_d = 4 \times 10^{-3}$	0.52	0.56	0.53	0.52	0.98	1.05	0.59	0.62	0.37	0.30
$C_d = 6 \times 10^{-3}$	0.40	0.44	0.42	0.40	0.75	0.98	0.61	0.64	0.38	0.29
$C_d = 8 \times 10^{-3}$	0.33	0.36	0.35	0.33	0.62	0.92	0.61	0.64	0.38	0.29
no wave drag	0.00	0.00	0.00	0.00	0.00	1.76	1.22	1.15	0.91	1.47
approx. wave drag	0.89	1.11	1.28	1.19	1.55	0.93	0.29	0.26	0.13	0.07
$\mathbf{F}_w + 25\%$	0.84	0.90	0.86	0.88	1.67	1.63	0.90	0.94	0.59	0.52
$\mathbf{F}_w + 50\%$	1.09	1.18	1.14	1.18	2.25	2.26	1.32	1.37	0.89	0.80
$\mathbf{F}_w + 75\%$	1.38	1.50	1.46	1.54	2.97	3.06	1.87	1.96	1.31	1.20
4 × 4 nm	0.65	0.71	0.69	0.77	1.24	0.97	0.50	0.48	0.37	0.17
1 × 1 nm	0.53	0.55	0.52	0.53	1.05	1.08	0.61	0.64	0.38	0.39
1995	0.61	0.63	0.54	0.51	0.96	1.36	0.66	0.58	0.33	0.28

Table 5. Spatial average in area B of dissipation by internal wave drag and bottom stress over sub-areas deeper than the depth given in the table

	Internal wave drag [mW m ⁻²]					Bottom stress [mW m ⁻²]				
	0 m	50 m	100 m	150 m	200 m	0 m	50 m	100 m	150 m	200 m
$C_d = 3 \times 10^{-3}$	0.29	0.28	0.19	0.14	0.10	0.50	0.41	0.15	0.10	0.11
$C_d = 1 \times 10^{-3}$	0.44	0.43	0.30	0.22	0.17	0.32	0.25	0.09	0.07	0.08
$C_d = 2 \times 10^{-3}$	0.34	0.34	0.23	0.16	0.12	0.44	0.35	0.13	0.09	0.10
$C_d = 4 \times 10^{-3}$	0.25	0.25	0.16	0.12	0.08	0.52	0.44	0.17	0.12	0.11
$C_d = 6 \times 10^{-3}$	0.20	0.20	0.13	0.10	0.07	0.55	0.47	0.19	0.13	0.12
$C_d = 8 \times 10^{-3}$	0.17	0.17	0.11	0.08	0.06	0.55	0.48	0.20	0.14	0.12
no wave drag	0.00	0.00	0.00	0.00	0.00	0.83	0.74	0.37	0.25	0.24
approx. wave drag	0.39	0.42	0.34	0.30	0.28	0.40	0.29	0.05	0.03	0.03
$\mathbf{F}_w + 25\%$	0.39	0.39	0.26	0.18	0.13	0.79	0.66	0.24	0.17	0.16
$\mathbf{F}_w + 50\%$	0.51	0.50	0.34	0.24	0.17	1.16	0.97	0.36	0.25	0.24
$\mathbf{F}_w + 75\%$	0.64	0.64	0.43	0.30	0.21	1.65	1.38	0.53	0.36	0.34
4 × 4 nm	0.30	0.29	0.20	0.17	0.14	0.56	0.39	0.13	0.08	0.09
1 × 1 nm	0.24	0.24	0.15	0.10	0.07	0.49	0.40	0.17	0.12	0.12
1995	0.36	0.36	0.25	0.18	0.12	0.78	0.67	0.27	0.18	0.18

Table 6. Spatial average in area C of dissipation by internal wave drag and bottom stress over sub-areas deeper than the depth given in the table

	Internal wave drag [mW m ⁻²]					Bottom stress [mW m ⁻²]				
	0 m	50 m	100 m	150 m	200 m	0 m	50 m	100 m	150 m	200 m
$C_d = 3 \times 10^{-3}$	0.23	0.25	0.27	0.29	0.44	1.55	0.43	0.32	0.21	0.17
$C_d = 1 \times 10^{-3}$	0.44	0.45	0.45	0.49	0.75	1.88	0.35	0.25	0.16	0.13
$C_d = 2 \times 10^{-3}$	0.29	0.31	0.33	0.36	0.55	1.67	0.41	0.30	0.19	0.16
$C_d = 4 \times 10^{-3}$	0.19	0.21	0.23	0.25	0.37	1.45	0.45	0.34	0.22	0.17
$C_d = 6 \times 10^{-3}$	0.15	0.17	0.18	0.20	0.29	1.32	0.46	0.35	0.24	0.17
$C_d = 8 \times 10^{-3}$	0.12	0.14	0.15	0.17	0.24	1.23	0.46	0.36	0.25	0.18
no wave drag	0.00	0.00	0.00	0.00	0.00	1.77	0.69	0.59	0.47	0.62
approx. wave drag	0.21	0.38	0.59	0.63	0.70	1.60	0.36	0.16	0.08	0.04
$\mathbf{F}_w + 25\%$	0.30	0.34	0.36	0.40	0.63	2.24	0.68	0.52	0.34	0.28
$\mathbf{F}_w + 50\%$	0.39	0.43	0.47	0.52	0.84	3.08	0.97	0.75	0.50	0.41
$\mathbf{F}_w + 75\%$	0.49	0.54	0.60	0.67	1.09	4.14	1.39	1.07	0.73	0.61
4 × 4 nm	0.28	0.30	0.32	0.40	0.44	1.65	0.45	0.32	0.20	0.11
1 × 1 nm	0.16	0.18	0.19	0.21	0.36	1.26	0.38	0.32	0.21	0.20
1995	0.26	0.28	0.28	0.29	0.40	1.85	0.62	0.40	0.26	0.21

Table 7. Spatial average in area D of dissipation by internal wave drag and bottom stress over sub-areas deeper than the depth given in the table.

	Internal wave drag [mW m ⁻²]					Bottom stress [mW m ⁻²]				
	0 m	50 m	100 m	150 m	200 m	0 m	50 m	100 m	150 m	200 m
$C_d = 3 \times 10^{-3}$	0.43	1.34	1.83	1.56	0.88	4.09	1.30	0.95	0.65	0.50
$C_d = 1 \times 10^{-3}$	0.76	2.25	2.97	2.55	1.34	4.84	1.04	0.72	0.53	0.35
$C_d = 2 \times 10^{-3}$	0.53	1.62	2.18	1.86	1.02	4.41	1.21	0.86	0.60	0.43
$C_d = 4 \times 10^{-3}$	0.37	1.16	1.61	1.38	0.79	3.86	1.36	1.01	0.69	0.55
$C_d = 6 \times 10^{-3}$	0.30	0.95	1.34	1.16	0.67	3.51	1.42	1.10	0.76	0.64
$C_d = 8 \times 10^{-3}$	0.25	0.82	1.17	1.02	0.60	3.27	1.46	1.16	0.82	0.70
no wave drag	0.00	0.00	0.00	0.00	0.00	4.48	2.32	2.20	1.63	1.11
approx. wave drag	0.56	2.59	4.42	4.33	3.80	4.00	0.81	0.31	0.25	0.28
$\mathbf{F}_w + 25\%$	0.55	1.72	2.37	2.04	1.16	5.88	1.91	1.41	0.98	0.77
$\mathbf{F}_w + 50\%$	0.68	2.14	2.96	2.57	1.49	7.94	2.65	1.98	1.39	1.11
$\mathbf{F}_w + 75\%$	0.84	2.63	3.66	3.20	1.88	10.61	3.58	2.72	1.94	1.58
4 × 4 nm	0.44	1.27	2.59	2.44	2.75	4.30	1.10	0.79	0.55	0.58
1 × 1 nm	0.38	1.23	1.41	0.98	0.48	3.92	1.45	0.96	0.66	0.55
1995	0.44	1.43	2.02	1.74	0.97	4.25	1.80	1.34	0.90	0.67

increases. Although changes are large in some areas, they are consistently so both for internal wave drag and bottom drag, indicating that although stratification was stronger, differences in wind forcing between the years is at least as important. Ranges in natural variability can be of the order of 25–50% in the dissipation by wave drag indicated by averages from the two years.

5. Discussion

We have shown that the transfer of energy from low-frequency, wind-forced barotropic motions to internal waves is potentially an important driver of diapycnal mixing in the Baltic Sea. However, we get an average dissipation from internal wave drag over stratified parts (depth > 50 m) of the Baltic proper of about 0.25 mW m^{-2} (Table 6), and that is substantially less than the required energy supply of 2.1 mW m^{-2} (Liljebladh & Stigebrandt 2000). The sensitivity study shows that this can be an underestimate and the model can give up to 0.4 mW m^{-2} without significantly reducing performance in reproducing observed sea levels. However, there are no simple means of further increasing the dissipation by internal wave drag, i.e. by increasing wind speeds or changing drag coefficients. The estimates of dissipation by internal wave drag at depth in areas A and B were compared to the required energy supply estimated by Axell (1998). He estimated that about 5 and 0.6 mW m^{-2} needed to be supplied to these areas below 150 m depth compared to the dissipation by internal waves of 0.62 and 0.14 mW m^{-2} . The sensitivity analysis indicates a large uncertainty in the dissipation here. Taking an extreme case: the dissipation in area A is quite sensitive to depth and wind forcing, so if we limit the average to deeper areas than 200 m and assume that wind stress should be increased by 50%, the dissipation becomes 2.25 mW m^{-2} . In the high-wind speed case, dissipation due to wave drag is about 0.24 mW m^{-2} in area B.

An uncertainty in the comparison between estimates of the energy supply required to explain the observed changes in stratification with our computations of the energy supply is that the former are calculated using an uncertain Richardson flux number (R_f), or mixing efficiency. Liljebladh & Stigebrandt (2000) used $R_f = 0.06$ and Axell (1998) used $R_f = 0.05$, but values up to $R_f = 0.17$, originating from Osborn (1980), are commonly used. Arneborg (2002) suggested an intermediate value of $R_f = 0.11$ from theoretical considerations, which was recently confirmed in laboratory experiments by Prastowo et al. (2009). In any case, differences by a factor of three in the various estimates of R_f may imply the even greater importance of the energy supply to mixing from wind-forced internal waves.

The parameterization of internal wave drag is derived from a much simplified theory, and the consequences of this need to be discussed. In the parameterization of wave drag force we neglect the fact that internal waves are generated on both sides of the step. The energy density of the waves on the shallow side is, however, much less than on the deep side. Interpreting the idealized analysis by St. Laurent et al. (2003), it seems that neglecting internal waves on the shallow side of the step may potentially underestimate the wave drag by some 20%.

The use of a simple quadratic law (eq. (5)) to parameterize the drag due to small-scale flow separation (form drag) and bed friction is rather crude. This is indeed quite true for the Baltic Sea, with its large variations in bottom depths and its very large areas of stratification. In the non-stratified case, there exist more complex parameterizations that are probably more accurate, e.g. Mofjeld (1988), but in the stratified regions a vertically resolved stratified model would be necessary for accurate predictions of bottom drag. Since any parameterization of bottom drag would involve free parameters due to the lack of information about the true bottom roughness, an uncertainty would still remain. Moreover, bottom drag would still predominantly occur in shallow regions, where current speeds are large and therefore have a dominant effect on coastal sea level.

The effects of the Earth's rotation are not taken into account, which could cast doubt on long-period oscillations. There are, however, examples of similar parameterizations being used to quantify internal wave generation from sub-inertial tides (e.g. Tanaka et al. 2007). The generation itself should be relatively well described by the non-rotating model if no interference occurs, and this would be the case if the waves dissipate at generation or at least within an oscillation period typical of the driving force. Our hypotheses are that the rough, complex topography favours rather rapid breaking of the internal waves and that the lack of phase-locked frequencies in the wind forcing further decreases the probability of interference. The ultimate test would naturally be a measurement programme that investigates the generation processes in the Baltic proper. Arneborg (2000) performed a derivation of internal wave generation at a sill in a channel from slowly oscillating barotropic flows, taking into account the generation of baroclinic Kelvin waves. The formula he obtained had the same functional dependence on stratification and barotropic flow as the original step model formulation (Stigebrandt 1976).

All the steps between the grid cells are treated as autonomous wave makers in that we do not consider any interaction between waves generated in adjacent cells. In support of this assumption, it was recently shown experimentally that two very closely spaced sills (about 1 km or 1/7 of the

internal Rossby radius) generated internal tides without interaction (Johnson et al. 2007). This result was obtained by comparing the theoretical energy transfer with observed tidal currents, sea level and stratification.

St. Laurent et al. (2003) showed that the calculations of internal tide generation using the step-model can be sensitive to the resolution. In our case, this would be manifested as sensitivity changes of the grid resolution used in the model. In our simulations, a change in grid size from 4, 2 and 1 nautical miles systematically decreased the average dissipation due to wave drag, but the total changes were not larger than the other uncertainties. The comparison of dissipation in the deep basins was also somewhat difficult because they are quite small, so using the 4×4 nm grid barely resolves the deeps. Also, there is no 1×1 nm resolution grid available, so this was constructed by interpolating the 2×2 nm grid and thus did not contain additional roughness that could be present on a finer scale. Thus, it was not possible with the present model set-up to make definite calculations regarding the sensitivity of the grid resolution to the internal wave generation parameterization itself, so this will have to be resolved in a future investigation.

Döös et al. (2004) proposed a parameterization of drag force in shallow water models that takes into account the loss due to flow separation resulting from resolved topographic obstacles. The functional form of the parameterization resembles wave drag. The discrete form of the drag force in the x-direction according to Döös et al. (2004), say F_D^x , is given by

$$F_D^x = -C_s |u| \frac{H_b - d}{\Delta_s} u. \quad (29)$$

This has clear similarities with the approximate wave drag derived in this paper (eq. (21)). The obvious difference between the drag forces is that the slope friction parameterization is scaled with the current speed, while the wave drag is scaled with the internal group speed. Given that Döös et al. (2004) found an optimal fit to observed sea level variations for C_s of between 15 and 26 and that the current speed is typically at least one order of magnitude less than the group velocity for long internal waves of the first mode, the two parameterizations give drag forces of a similar order of magnitude. We did not repeat the detailed calibration to observed sea levels that Döös et al. (2004) performed, but according to our results, using the approximate wave drag does not improve the model's capability to reproduce the observed sea level time-series. The cause of this discrepancy is most probably that the primary influence on sea levels comes from drag in shallow regions in straits and close to coasts, and here the approximate wave drag is zero in contrast to the slope-friction.

Acknowledgments

Meteorological data were provided by the BALTEX hydrological data centre at the Swedish Meteorological and Hydrological Institute; sea level, stratification and current data were provided by the Swedish Meteorological and Hydrological Institute, the Finnish Marine Institute and the Danish Meteorological Institute. We thank Dr. Lars Arneborg and Prof. Anders Stigebrandt for the fruitful discussions and their valuable comments on earlier versions of this paper.

References

- Arakawa A., Lamb V. R., 1981, *A potential enstrophy and energy conserving scheme for the shallow water equations*, Mon. Weather Rev., 109 (1), 18–36.
- Arbic B. K., Garner S. T., Hallberg R. W., Simmons H. L., 2004, *The accuracy of surface elevations in forward global barotropic and baroclinic tide models*, Deep-Sea Res. Pt. II, 51 (25–26), 3069–3101.
- Arneborg L., 2000, *Oceanographic studies of internal waves and diapycnal mixing*, Ph.D. thesis A59, Earth Sci. Cent., Univ. Gothenburg, Sweden.
- Arneborg L., 2002, *Mixing efficiencies in patchy turbulence*, J. Phys. Oceanogr., 32 (5), 1496–1506.
- Axell L. B., 1998, *On the variability of Baltic Sea deepwater mixing*, J. Geophys. Res., 103 (C10), 21 667–21 682.
- Berntsen J., Xing J., Davies A. M., 2008, *Numerical studies of internal waves at a sill: Sensitivity to horizontal grid size and subgrid scale closure*, Cont. Shelf Res., 28 (10–11), 1376–1393.
- Döös K., Nycander J., Sigray P., 2004, *Slope-dependent friction in a barotropic model*, J. Geophys. Res., 109 (C01008), doi:10.1029/2002JC001517.
- Dyer K. R., 1986, *Coastal and estuarine sediment dynamics*, John Wiley & Sons Ltd., Chichester, 358 pp.
- Egbert G. D., Ray R. D., Bills B. G., 2004, *Numerical modeling of the global semidiurnal tide in the present day and in the last glacial maximum*, J. Geophys. Res., 109 (C03003), doi:10.1029/2003JC001973.
- Flather R. A., 1976, *A tidal model of the northwest European continental shelf*, Mem. Soc. Roy. Sci. Liege, Ser. 6th, Vol. 10, 141–160.
- Gustafsson B. G., Andersson H. C., 2001, *Modeling the exchange of the Baltic Sea from the meridional atmospheric pressure difference across the North Sea*, J. Geophys. Res., 106 (C9), 19 731–19 744.

- Gustafsson K. E., 2001, *Computations of the energy flux to mixing processes via baroclinic wave drag on barotropic tides*, Deep-Sea Res. Pt. I, 48 (10), 2283–2295.
- Jakobsen F., Azam M. H., Mahboob-Ul-Kabir M., 2002, *Residual flow in the Meghna Estuary on the coastline of Bangladesh*, Estuar. Coast. Shelf Sci., 55 (4), 587–597.
- Jayne S. R., St. Laurent L. C., 2001, *Parameterizing tidal dissipation over rough topography*, Geophys. Res. Lett., 28 (5), 811–814.
- Johnsson M., Green J. A. M., Stigebrandt A., 2007, *Baroclinic wave drag from two closely spaced sills in a narrow fjord as inferred from basin water mixing*, J. Geophys. Res., 112 (C11002), doi:10.1029/2006JC003694.
- Kuzmina N., Rudels B., Stipa T., Zhurbas V., 2005, *The structure and driving mechanisms of the Baltic intrusions*, J. Phys. Oceanogr., 35 (6), 1120–1137.
- Liljebladh B., Stigebrandt A., 2000, *The contribution of the surface layer via internal waves to the energetics of deepwater mixing in the Baltic*, Paper III Ph.D. thesis A56, Earth Sci. Cent., Univ. Gothenburg, Sweden.
- Martinsen E. A., Engedahl H., 1987, *Implementation and testing of a lateral boundary scheme as an open boundary-condition in a barotropic ocean model*, Coast. Eng., 11 (5–6), 603–627.
- Meier H. E. M., 2005, *Modeling the age of Baltic Sea water masses: Quantification and steady state sensitivity experiments*, J. Geophys. Res., 110 (C02006), 1–14.
- Meier H. E. M., Feistel R., Piechura J., Arneborg L., Burchard H., Fiekas V., Golenko N., Kuzmina N., Mohrholz V., Nohr C., Paka V. T., Sellschopp J., Stips A., Zhurbas V., 2006, *Ventilation of the Baltic Sea deep water: A brief review of present knowledge from observations and models*, Oceanologia, 48 (S), 133–164.
- Merrifield M. A., Holloway P. E., 2002, *Model estimates of M2 internal tide energetics at the Hawaiian Ridge*, J. Geophys. Res., 107 (C8), doi:10.1029/2001JC000996.
- Niwa Y., Hibiya T., 2001, *Numerical study of the spatial distribution of the M₂ internal tide in the Pacific Ocean*, J. Geophys. Res., 106 (C10), 22441–22449.
- Nycander J., 2005, *Generation of internal waves in the deep ocean by tides*, J. Geophys. Res., 110 (C10028), doi:10.1029/2004JC002607.
- Osborn T., 1980, *Estimates of the local rate of vertical diffusion from dissipation measurements*, J. Phys. Oceanogr., 10 (1), 83–89.
- Press W. H., Teukolsky S. A., Vetterling W. T., Flannery B. P., 1997, *Numerical recipes*, 2nd edn., Cambridge Univ. Press, Cambridge, 963 pp.
- Samuelsson M., Stigebrandt A., 1996, *Main characteristics of the long-term sea level variability in the Baltic Sea*, Tellus A, 48 (5), 672–683.
- Seifert T., Tauber F., Kayser B., 2001, *A high resolution spherical grid topography of the Baltic Sea – revised edition*, Proc. Baltic Sea Sci. Cong., 25–29 Nov. 2001, Stockholm, poster No 147.

- Simmons H. L., Hallberg R. W., Arbic B. K., 2004, *Internal wave generation in a global baroclinic tide model*, Deep-Sea Res. Pt. II, 51 (25–26), 3043–3068.
- Sjöberg B., Stigebrandt A., 1992, *Computations of the geographical distribution of the energy flux to mixing processes via internal tides and the associated vertical circulation in the ocean*, Deep-Sea Res., 39 (2A), 269–291.
- Smith S. D., 1980, *Wind stress and heat flux over the ocean in gale force winds* J. Phys. Oceanogr., 10 (5), 709–726.
- Soulsby R., 1997, *Dynamics of marine sands – A manual for practical applications*, Thomas Telford, London, 249 pp.
- St. Laurent L., Stringer S., Garrett C., Perrault-Joncas D., 2003, *The generation of internal tides at abrupt topography*, Deep-Sea Res. Pt. I, 50 (8), 987–1003.
- Stacey M. W., 1984, *The interaction of tides with the sill of a tidally energetic inlet*, J. Phys. Oceanogr., 14 (6), 1105–1117.
- Stigebrandt A., 1976, *Vertical diffusion driven by internal waves in a sill fjord*, J. Phys. Oceanogr., 6 (4), 486–495.
- Stigebrandt A., 1980a, *Barotropic and baroclinic response of a semi-enclosed basin to barotropic forcing from the sea*, [in:] *Fjord oceanography*, H. J. Freeland, D. M. Farmer & C. D. Levings (eds.), Plenum, New York, 151–164.
- Stigebrandt A., 1980b, *Some aspects of tidal interactions with fjord constrictions*, Estuar. Coast. Mar. Sci., 11 (2), 151–166.
- Stigebrandt A., 1999, *Resistance to barotropic tidal flow in straits by baroclinic wave drag*, J. Phys. Oceanogr., 29 (2), 191–197.
- Stigebrandt A., 2001, *Physical oceanography of the Baltic Sea*, [in:] *A systems analysis of the Baltic Sea*, F. Wulff, L. Rahm & P. Larsson (eds.), Springer Verlag, Heidelberg, 19–74.
- Stigebrandt A., 2003, *Regulation of vertical stratification, length of stagnation periods and oxygen conditions in the deeper deepwater of the Baltic proper*, Meereswiss. Ber., 54, 69–80.
- Stigebrandt A., Aure J., 1989, *Vertical mixing in basin waters of fjords*, J. Phys. Oceanogr., 19 (7), 917–926.
- Stigebrandt A., Lass H. U., Liljebladh B., Alenius P., Piechura J., Hietala R., Beszczyńska A., 2002, *DIAMIX – An experimental study of diapycnal deepwater mixing in the virtually tideless Baltic Sea*, Boreal Environ. Res., 7 (4), 363–369.
- Svensson A., 2005, *Observations of baroclinic eddies in the Baltic Sea*, Tech. Rep. B472, Dept. Oceanogr., Univ. Gothenburg.
- Tanaka Y., Hibiya T., Niwa Y., 2007, *Estimates of tidal dissipation and diapycnal diffusivity in the Kuril Straits using TOPEX/POSEIDON altimeter data*, J. Geophys. Res., 112 (C10021), doi:10.1029/2007JC004172.
- Tanaka Y., Hibiya T., Niwa Y., 2007, *Estimates of tidal energy dissipation and diapycnal diffusivity in the Kuril Straits using topeX/poseidon altimeter data*, J. Geophys. Res., 112 (C10), 1–9.

- Umgiesser G., 1997, *Modelling the Venice Lagoon*, Int. J. Salt Lake Res., 6 (2), 175–199.
- Verboom G. K., de Ronde J. G., van Dijk R. P., 1992, *A fine grid tidal flow and storm surge model of the North Sea*, Cont. Shelf Res., 12 (2–3), 213–233.
- Weis P., Thomas M., Sündermann J., 2008, *Broad frequency tidal dynamics simulated by a high resolution global ocean tide model forced by ephemerides*, J. Geophys. Res., 113 (C10029), doi:10.1029/2007JC004556.
- Williamson J., 1980, *Low-storage Runge-Kutta schemes*, J. Comput. Phys., 35 (1), 48–56.